Nano Energy 88 (2021) 106284

Contents lists available at ScienceDirect

Nano Energy

journal homepage: www.elsevier.com/locate/nanoen

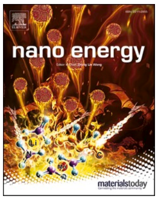

Boosting power output of flutter-driven triboelectric nanogenerator by flexible flagpole

Yi Zhang, Sau-Chung Fu [*], Ka Chung Chan, Dong-Myeong Shin, Christopher Y.H. Chao

Department of Mechanical Engineering, The University of Hong Kong, Hong Kong, China

A R T I C L E I N F O

Keywords:
Triboelectric Nanogenerators
Wind Energy
Fluttering phenomenon
Flagpole
Wireless Sensor Node

A B S T R A C T

One important component of Industry 4.0 is the Internet of Things (IoT) which links every "things" by distributed wireless sensor nodes (WSNs). Most sensor nodes are small in size, consume little energy and are adaptive to the environment. Small and local power generation is desirable for such WSNs, and harvesting energy from ambient wind is one of the potential methods. To harvest small-scale wind energy effectively, a promising device called flutter-driven triboelectric nanogenerator (FTENG) was lately developed, which converts kinetic energy in the self-fluttering motion of a flag to electricity. Many studies focused on material development to increase the surface charge density of the surfaces to enhance the energy output of FTENG, but few tried to enlarge the fluttering motion by considering the structural design. This study shows that by simply replacing the rigid flagpole in the FTENG with a flexible flagpole, the energy output is enhanced. The fluttering dynamics of the flags with rigid and flexible flagpoles was recorded by high-speed camera. It was found that when the flag was held by a flexible flagpole, the fluttering amplitude and the contact area between the flag and electrode plates were increased. The channel width, flag thickness, and flag length in relation to the voltage, current and power outputs were also investigated in this study. The greatest enhancement can reach 113 times when the wind velocity is 10 m/s. In a demonstration experiment, the device can light 254 LEDs and a temperature and humidity wireless sensor. In addition, the device has a stable output in a one-hour durability test. Comparing with other FTENGs from the literatures, our device has a lower critical velocity and a higher energy output. Besides, our design was integrated into other FTENG structures and got an enhancement of more than two folds in power density. This work demonstrates the use of a flexible flagpole to enhance the output performance of an FTENG by increasing the fluttering mechanical energy and increasing the contact area. Based on the performance obtained in this study, the improved FTENG has the potential to be applied in smart cities as a power source for IoT WSNs.

1. Introduction

In order to provide continuous power for distributed IoT Wireless Sensor Nodes (WSNs), the development of small-scale energy harvesting devices, which convert ambient energy into electricity, is desired [1–9]. Wind energy is one of the feasible energy sources since it is clean, sustainable, and ubiquitous. The available space for installing a wind energy harvester to power WSNs is limited. However, miniaturization of traditional electromagnetic generator (EMG) based wind turbines increases the viscous and mechanical losses, which make the energy output too low to match their operating cost [10]. Flutter-driven triboelectric nanogenerator (FTENG) is an innovative technology that harvests small-scale wind energy by utilizing the natural phenomenon of a flexible object oscillating in the flow [11–13]. Due to its low cost, lightweight and easy fabrication process [14], FTENG exhibits great potential in the application to power IoT WSNs, which have a power budget of ~0.001–100 mW, depending on the data rates and system architecture [15–18].

A variety of structures and materials have been developed and proposed to enhance the conversion efficiency of FTENGs. The first FTENG was developed by Yang et al. [19] in 2013. By utilizing the periodic fluttering of fluorinated ethylene-propylene (FEP) film between two aluminium foils, they designed a FTENG that could light tens of LEDs and detect the wind direction and speed. To fully convert the fluttering flag energy, Wang et al. [20] designed a FTENG structure that has two TENGs in a FTENG device. The peak output of their device was about 3.7 mW and this device could produce continuous DC power for a WSN. However, there are two drawbacks of the present FTENG, which hinder

---

[*] Correspondence to: Department of Mechanical Engineering, the University of Hong Kong, Pokfulam Road, Hong Kong.
E-mail address: scfu@hku.hk (S.-C. Fu).

https://doi.org/10.1016/j.nanoen.2021.106284
Received 18 April 2021; Received in revised form 7 June 2021; Accepted 21 June 2021

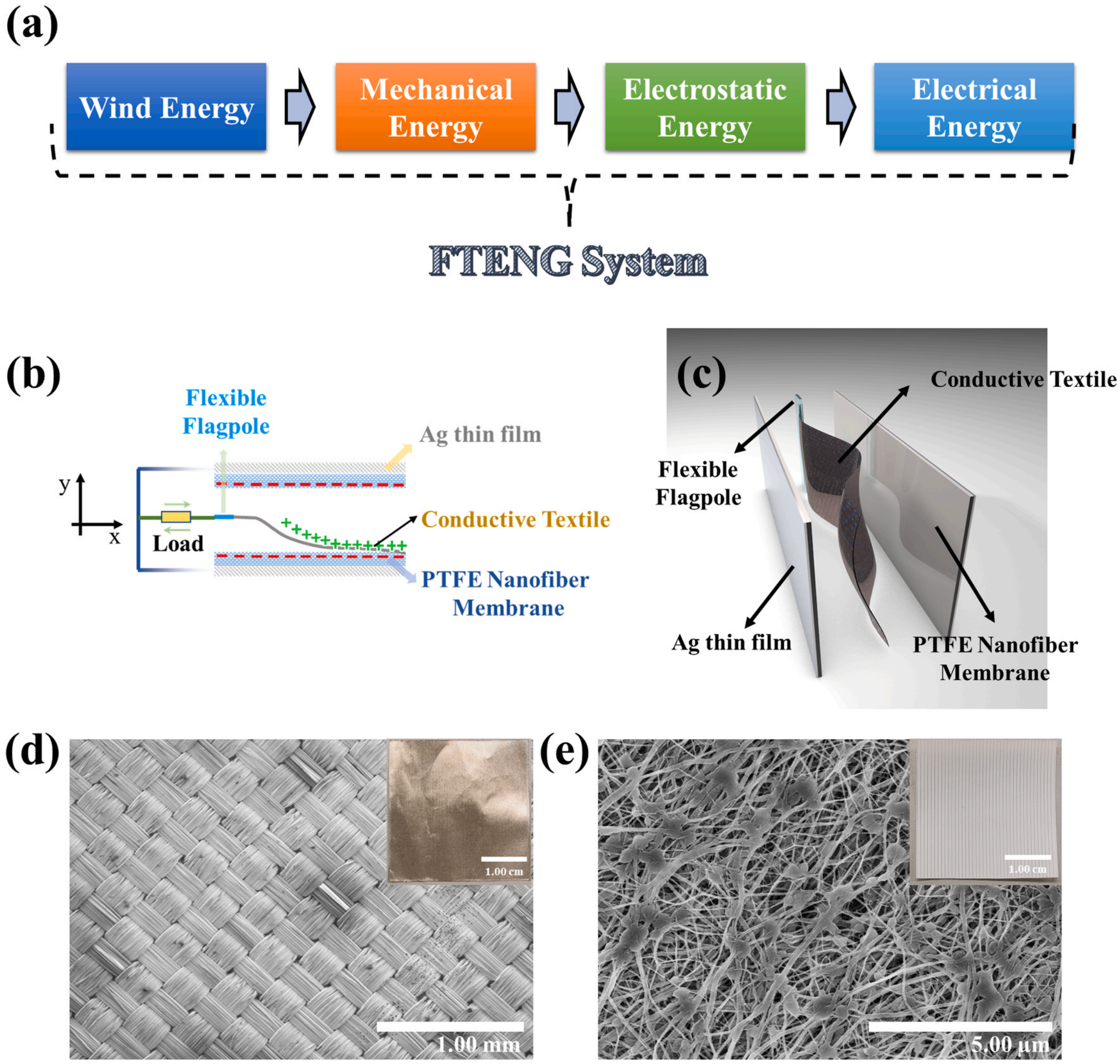

Fig. 1. (a) The energy flow of a FTENG system; (b) Schematic cross-sectional view of the fabricated FF-FTENG and electric wires connections; (c) Three-dimensional schematic diagram of FF-FTENG; SEM images of (d) knitted conductive textile and (e) PTFE nanoporous membrane; inside figures are photos of conductive textile and PTFE membrane, respectively.

its further development: 1. high critical velocity (or cut-in velocity in wind turbine research) that activates the flutter and 2. low energy output. To obtain low critical velocity, the flag material needs to be thin, light and flexible, but it also needs to be mechanically strong to sustain the strong wind flow. Conductive textile (CT) is a potential candidate and has been used as flag material in previous studies [21,22]. Bae et al. [21] developed a CT-based FTENG, which exhibits an open-circuit voltage (V_{oc}) of 200 V and a short-circuit current (I_{sc}) of 60 μA with a flag size of 7.5 cm × 5 cm at wind speed of 15 m/s. The FTENG has an average power of 0.86 mW. Later, Dudem et al. [22] developed a FTENG using CT as both flag and floating electrode. At wind speed of 10 m/s, the FTENG produced V_{oc} of ~39 V and I_{sc} of ~3 μA. The peak power density was 5.12 mW/m^2, and more importantly, their device had low critical velocity down to 1.2 m/s. The critical velocity has been greatly decreased using CT as the fluttering flag. However, the energy output of the FTENG with CT as a fluttering flag was not high and required further improvement, so that the device could power more sensors under moderate wind velocity in ordinary environments.

Normally, only the trailing section near the free end of the fluttering flag contributes to the energy generation in FTENG because it is the only part that encounters the sidewalls for triboelectric effect. As for the leading section of the flag, the fluttering amplitude is small. The kinetic energy of the leading section cannot be transferred to electrical energy by triboelectrification since the leading section of the flag cannot contact the sidewalls. Handful research attempted to solve this conundrum. Wang et al. [23] reported a hybridized nanogenerator using an EMG to harvest the kinetic energy of the leading section of the flag. However, the fluttering energy in the leading section was small. There was only little energy that could be extracted using EMG in the leading section. Moreover, the addition of EMG into the system increases the complexity of the power management system, since the two generators have different impedance. From an energy conversion point of view (as shown in Fig. 1(a)), there are three conversions (the detailed three steps are explained in Note S1 in Supplementary Materials) from the wind energy source to the electrical energy output. It is important to convert more mechanical energy from the wind to the flag, so the flag has more energy to impact on the sidewalls for contact electrification process and to overcome the electrostatic force when detaching from the walls for the electrostatic induction process. Therefore, a technique that can amplify the mechanical energy of the fluttering flag and use the energy of the leading section of the flag is important to improve the energy output of the FTENG [24–28]. There are three major components, i.e., flag, sidewalls, and flagpole, in a FTENG system. More attentions have been attracted to the novel design of flag and sidewalls. However, to the author’s knowledge, no study investigates the influence of flagpole on the energy output of the FTENG. As the holder sustains the flag in the

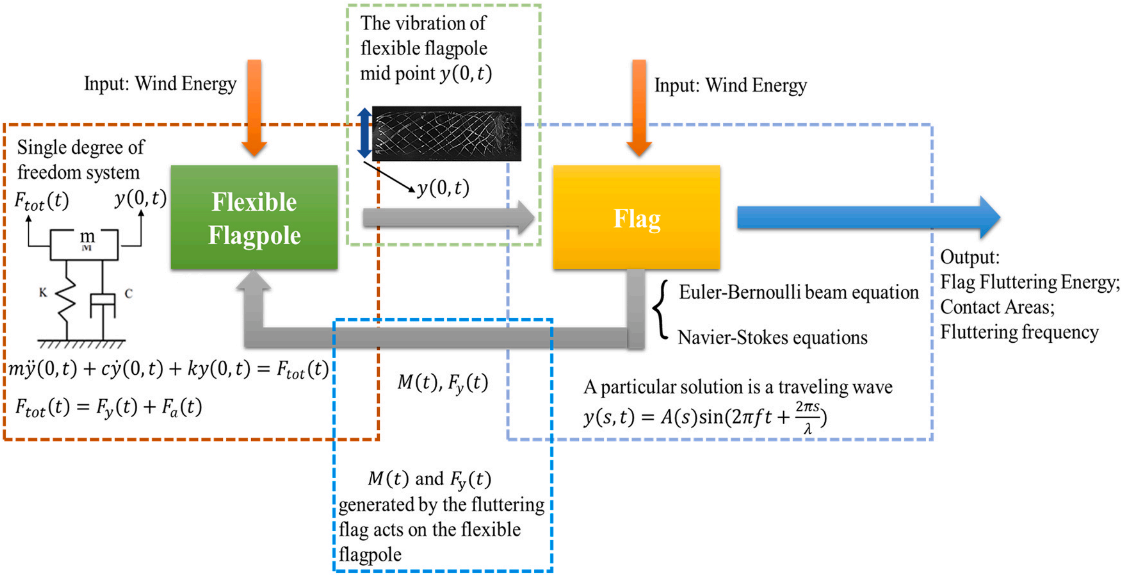

Fig. 2. A schematic diagram to illustrate the interaction among wind, flexible flagpole and flag.

wind, the flagpole receives drag force and lift force generated from the fluttering flag. The lift force on the flag applies a flapping moment and a force on the flagpole, which induces rotation and transverse vibration, respectively. Virot et al. [29–32] studied the unsteady drag force and the flapping moment around the flagpole. They concluded that the flapping moment is periodic and related to the fluttering modes of the flags. It occurred to us that the force and moment applied on the flagpole can be utilized to make the flagpole vibrate, in turn, amplify the fluttering motion of the whole flag, and therefore increase the contact areas between the flag and sidewalls.

In this study, we proposed to replace the rigid flagpole with a flexible flagpole in FTENGs using CT as the fluttering flag. The objective of this study is to explore the potential of substituting the rigid flagpole with a flexible flagpole in a FTENG to amplify the fluttering motion, enlarging the contact areas and hence boosting the power output. The FTENG with flexible flagpole will be hereinafter referred as FF-FTENG (Flexible Flagpole-Flutter-driven Triboelectric Nanogenerator). In contrast, the FTENG with rigid flagpole will be called RF-FTENG. The fluttering dynamics was studied using a high-speed camera and was used to explain the mechanism of motion amplification introduced by the flexible flagpole. The influence of the flag's thickness, the channel width and the flag length on the energy output, critical velocity, threshold velocity were also investigated. The critical and threshold velocities are important for the FF-FTENG. The critical velocity is the velocity where the flag starts to flutter when the wind speed slowly increases. The threshold velocity is the velocity where the flagpole starts to flutter and the V_{oc} and I_{sc} of the FF-FTENG increase with a much higher gradient. The optimal flag length on energy output has been determined for FF-FTENG. By using a power management module, the FF-FTENG can continuously produce a direct current with a constant voltage of about 1.9–3.3 V to directly and sustainably power a WSN. This work proposed an effective and simple approach to boost the energy output of the FTENG, and this approach can be applied to other FTENG structures.

2. Methodologies

The device structure of a FF-FTENG is depicted in Fig. 1(b) and (c). Some multi-angle photographs of FTENG are shown in Fig. S1 in Supplementary Materials. Fluttering flags with three thicknesses, 20 μm, 30 μm and 70 μm, were used in this study, and they were made by copper-nickel coated polyester fabric conductive textile (as shown in Fig. 1(d)). All flags were 45 mm wide (H). The flag was sustained by a flexible flagpole made of polyethylene terephthalate (PET) with thickness of 0.2 mm and width of 20 mm in the middle of the channel. In contrast, the case of a rigid flagpole, which was made of glass with thickness of 1 mm, was also tested. The Young's modulus of glass (50–90 GPa) is higher than that of PET (2.8–3.2 GPa) by one order of magnitude [33,34]. Polytetrafluoroethylene (PTFE) nanofiber membranes (a commercial electrospinning membrane, Sterlitech PTFE23001, 0.2 μm, as shown in Fig. 1(e)) with a thin layer of evaporation deposited silver were attached to the two sides of the channel walls as electrodes. The FF-FTENG was a contact-separation mode TENG. In this contact-separation mode TENG, the tribo-positive material was the CT and the tribo-negative materials were the PTFE nanofiber membranes, which is almost the most tribo-negative material in the triboelectric series. Surface morphologies of the CT and PTFE nanofiber membranes were observed using a field-emission scanning electron microscope (FESEM; S-4800 FEG, Hitachi, Japan). The flag is conductive, and therefore, the electric wires can be connected to the flag as shown in Fig. 1(b). The working mechanism is the same as the FTENG described in Dudem et al. [22]. Briefly, when the CT flag flutters between the two side walls, an alternating current will be induced in the external circuit resulting from the contact electrification and electrostatic induction. The conductive flag can also serve as a floating electrode. The schematic diagram of power generation principle of FF-FTENG can be found in Fig. S2 in the Supplementary Materials.

The major difference between the FF-FTENG and an RF-FTENG is the involvement of interaction among wind, flexible flagpole and flag, as illustrated in Fig. 2. To model the motion of the fluttering flag, the Euler-Bernoulli beam equations and Navier-Stokes equations can be used [24]. It can be described as a traveling harmonic wave, $y(s,t)$. When the wind velocity exceeds the critical velocity, the flutter of the flag generates a periodic flapping moment $M(t)$ and a periodic aerodynamic force in y-direction $F_y(t)$ acting on the flagpole. If the flagpole is flexible, the force and moment will force the flagpole to vibrate. In addition, the flexible flagpole can also vibrate by itself under the aerodynamics force ($F_a(t)$) due to the fluid-structure interaction (galloping effect). The motion of the flagpole can be modelled as a single degree of freedom system (SDOF) and will be the boundary condition, $y(0,t)$, for solving the fluttering flag equation. Thus, the interaction among wind, flexible flagpole and flag forms a closed loop control system. The vibration of the flagpole amplifies the fluttering motion of the flag leading to a larger contact area between the flag and the sidewalls. Therefore, a larger electrical output is expected to be generated. Future work is needed to

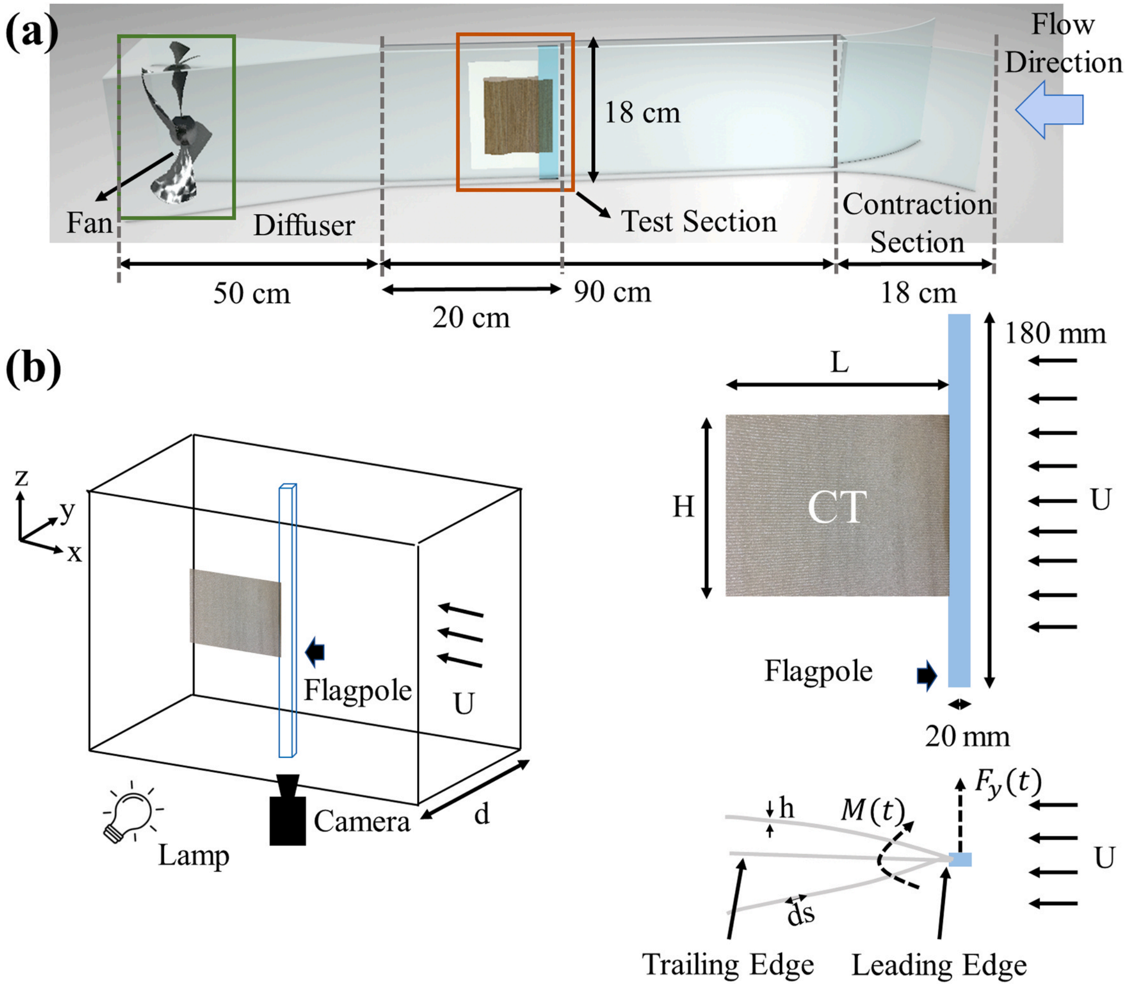

Fig. 3. (a) Schematic diagram of the experimental setup and the FF-FTENG installed in a custom-made wind tunnel; (b) Dimensions of the flag, flagpole and wind channel.

use some numerical simulations to solve the physical model.

A custom-made wind tunnel was built of acrylic to provide a uniform wind speed (as illustrated in Fig. 3(a)). The cross section of test section in the wind tunnel has a height of 180 mm and a changeable width from 10 mm to 30 mm. The flag was stuck on a flagpole as shown in Fig. 3(b) and positioned in the middle of the channel. To demonstrate the energy-boosting effect of the flexible flagpole and study the relationship between the electrical output and the wind velocity, an experiment was designed using wind velocities varying from 0 m/s to 12.21 m/s. The wind velocity range covers almost all winds in daily lives. The Beaufort scale for wind velocity categories is shown in Table S1 in the Supplementary Materials for reference. A high-speed camera (Phantom VEO 410 L, 512*128 pixels, 6.0 pixels/mm, 1000–4000 frames per second (fps)) was employed to record the flag's fluttering motion with the illumination of a 30 W LED lamp. The flag's surface was painted black and the edges were painted white for higher contrast for easier observation. Snapshot superimpositions and fluttering dynamics were analyzed by an imaging-processing software called ImageJ. The output current was measured by an electrometer (Keithley 6514), and the output voltage was analyzed by a digital oscilloscope (Tektronix TDS 2024C) with a high voltage probe (Tektronix P5100A) with 40 MΩ input impedance. The root mean square (RMS) output values were used in the analysis, as they are vital to access the effective available output power.

3. Results and discussion

3.1. The performance of FF-FTENG under different wind velocity

Before presenting the results of FF-FTENG, the governing equations for V_{oc} and I_{sc} in a contact-separation mode TENG based on the parallel plate capacitor model are firstly introduced [35]. The detailed derivation process can be found in Note S2 in the Supplementary Materials.

$$V_{oc} = \frac{\sigma x_{max} \cdot \sin(2\pi f t)}{\varepsilon_0} \tag{1}$$

$$I_{sc} = \frac{2\pi S \sigma d_0 x_{max} \cos(2\pi f t)}{(d_0 + x_{max} \cdot \sin(2\pi f t))^2} \cdot f \tag{2}$$

where S is the size of contact area, σ is the triboelectric surface charge density, Q is the amount of transferred charges between the two triboelectric layers, ε_0 is the permittivity of vacuum, d_0 is the effective thickness of the dielectric layer, $x(t)$ is the distance between the two triboelectric layers, x_{max} is the maximum separation distance and f is the contact-separation frequency.

These equations are for surfaces moving parallel to each other. On the other hand, in the case of FTENG, the flag does not move parallel to the sidewalls, which increases the complexity and difficulties of the problem. Thus, these governing equations cannot be directly applied to the case of FTENG but can help to explain the experimental results in general. It should be noted that V_{oc} is directly proportional to the

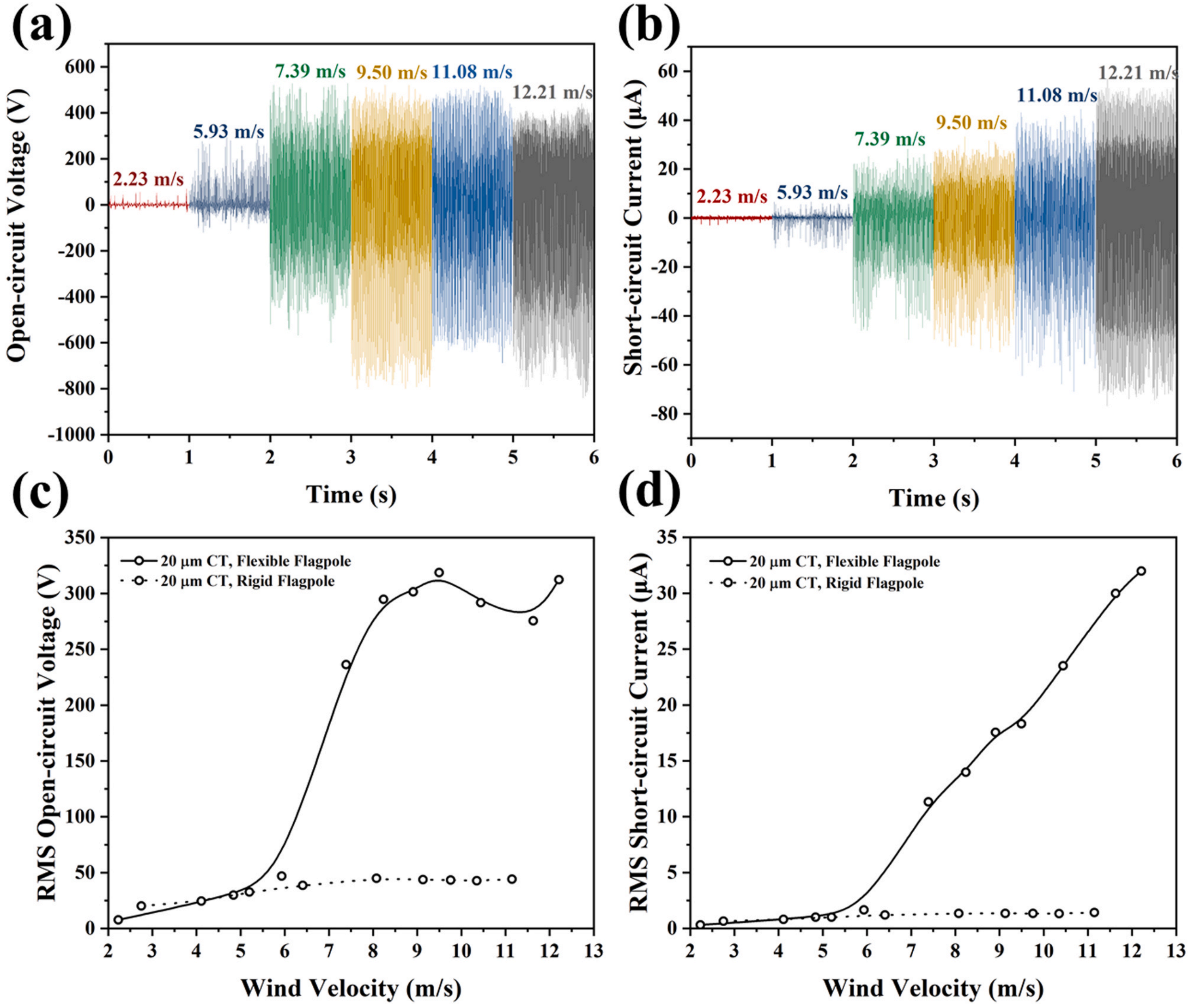

Fig. 4. The electrical output performance of the FF-FTENG. The thickness of the flag is 20 μm (a) Open-circuit voltage and (b) short-circuit current of the FF-FTENG; (c) RMS open-circuit voltage and (d) RMS short-circuit current of the FF-FTENG and RF-FTENG with the same dimensions under different wind velocities.

maximum contact-separation distance and surface charge density, and I_{sc} is directly proportional to the contact areas, surface charge density and contact-separation frequency.

To study the influence of wind velocity on the performance of FTENG, both rigid and flexible flagpoles were tested using flags with thickness (h) of 20 μm. The result is shown in Fig. 4. Fig. 4(a) and (b) show the V_{oc} and I_{sc} of the FF-FTENG under different wind velocities, respectively. Fig. 4(c) and (d) show the RMS open-circuit voltage ($V_{oc,RMS}$) and RMS short-circuit current ($I_{sc,RMS}$) for the FF-FTENG and RF-FTENG. The flag in FF-FTENG lost its stability and started to flutter after the critical velocity (2.23 m/s at this case), while the flag in RF-FTENG started to flutter at 2.75 m/s. With the increase in wind velocity, the $V_{oc,RMS}$ increased as higher wind speed resulted in larger contact forces between flag and sidewalls and therefore higher surface charge density was generated. The increasing rate of $V_{oc,RMS}$ remained unchanged until 5.93 m/s when $V_{oc,RMS}$ increased to 46.87 V. Then, there was a magnification of the increment rate because the flexible flagpole started to flutter at 5.93 m/s (threshold velocity in this case), and therefore, the flag fluttered not only at the trailing section, but also at the leading section. The $V_{oc,RMS}$ increased dramatically to 236.31 V when the wind velocity reached 7.39 m/s, and $V_{oc,RMS}$ reached a maximum of 318.62 V at the wind velocity of 9.50 m/s. Then, the value for $V_{oc,RMS}$ was steady with a small fluctuation from 9.50 m/s to 12.21 m/s and the value was about 300 V. On the other hand, the variation of the current output experienced a different trend. The current output monotonically increased with the wind velocities after the threshold velocity. It is clearly seen that the increasing gradient is much higher after the threshold velocity. The $I_{sc,RMS}$ was 1.66 μA at a velocity of 5.93 m/s, and reached a maximum $I_{sc,RMS}$ of 31.99 μA at a velocity of 12.21 m/s. The reason that voltage was steady with a small fluctuation while the current continuously increased from 9.50 m/s to 12.21 m/s is explained as following. From Eqa. (1) and (2), the I_{sc} increased as the wind velocity increased since the I_{sc} is directly proportional to the fluttering frequency. As the wind velocity increased, the fluttering frequency increased linearly as demonstrated in Fig. 5(c) and Fig. S3 in Supplementary Materials in the later content. However, the steady V_{oc} (RMS value at 300 V and peak value at 800 V) may be attributed to the surface charge density which reached a saturation value [24,36]. As the wind speed increased, the contact force between the fluttering flag and the sidewalls also increased. Due to a higher contact force, the surface charge density is higher. However, after a certain wind speed, the charge density on the PTFE sidewalls reaches a saturated state, and therefore the voltage reaches a maximum value and be steady with a small fluctuation.

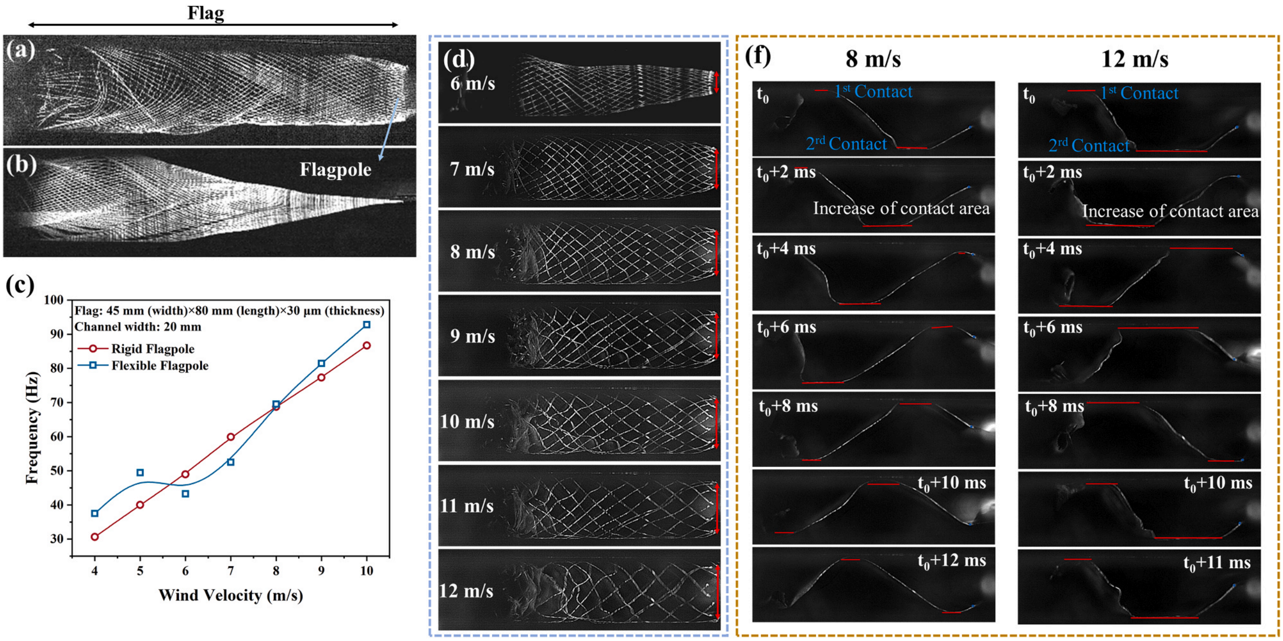

Fig. 5. The fluttering dynamics comparison between the flag with (a) a flexible flagpole and (b) a rigid flagpole (L=80 mm, H=45 mm, h=30 μm, d=20 mm, U=10 m/s); (c) The fluttering frequency of a flag in the FF-FTENG and RF-FTENG corresponding to the increasing flow velocity; (d) Snapshot superimpositions of FF-FTENG at different wind velocities from 6 m/s to 12 m/s; (e) Snapshots of FF-FTENG under 8 m/s and 12 m/s, there are two contacts for the flag and sidewalls all the time.

3.2. *The fluttering motion of a flag with flexible flagpole*

The electricity is generated by the wind-induced contact-separation behavior between the flag and the two electrode plates, thus it is essential to understand the detailed dynamic characteristics of flutters. The flags' fluttering dynamics with both types of flagpoles were captured by the high-speed camera at 4000 fps and are shown in Fig. 5. The flags have a thickness (h) of 30 μm, and the channel width (d) is 20 mm. For the flexible flagpole case, the fluttering motion took place on the whole flag from the leading edge to the trailing edge, and the fluttering amplitude quickly increased to the width of the channel as shown in Fig. 5(a) and Movie S1. In contrast, when the flagpole was rigid, the fluttering amplitude gradually increased as shown in Fig. 5(b). After the wind velocity exceeds the critical velocity, the fluttering of flag generated a flapping moment ($M(t)$ in Fig. 3(b)) and a force ($F_y(t)$ in Fig. 3(b)) on the flagpole. If the flagpole is flexible, the flapping moment applied on the flagpole forces it to vibrate. The flexible flagpole can also vibrate by itself under wind due to galloping effect. Combined with these two effects, the vibration of the flagpole amplified the fluttering motion of the whole flag, and therefore led to a larger contact area of the flag taken part in the electrification process. Therefore, a larger electrical output was generated. In addition, according to Fig. 5(c), the fluttering frequency of FF-FTENG was slightly higher than that of RF-FTENG, which further improved the energy output [28]. Fig. 5(d) shows the

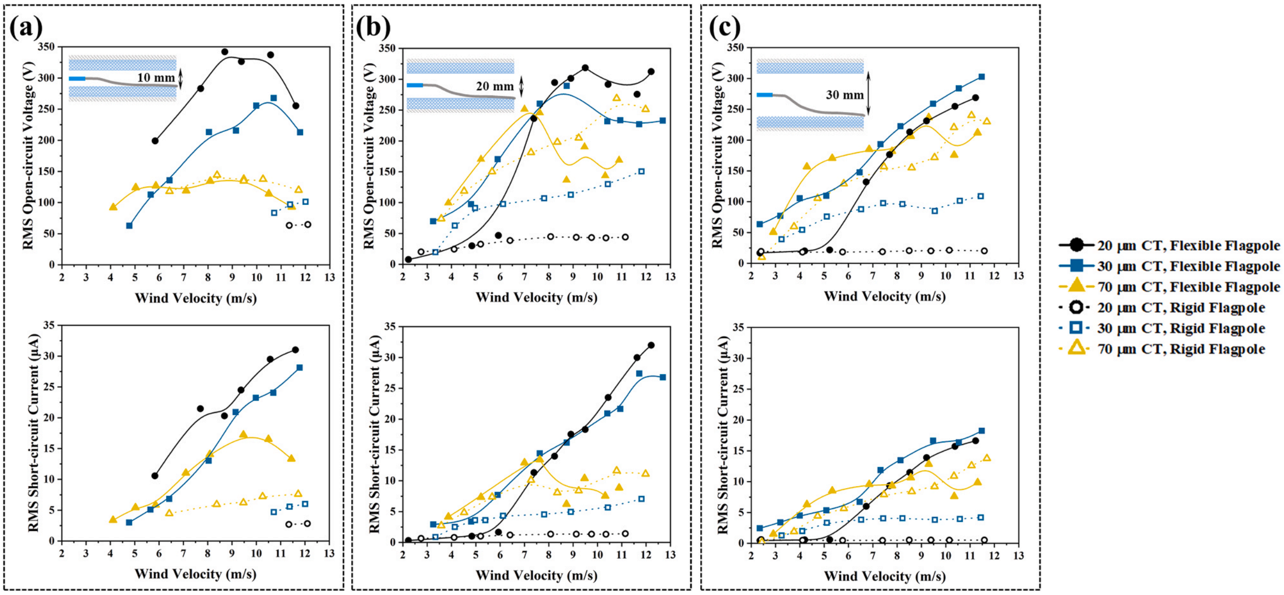

Fig. 6. Dependence of the generated RMS open-circuit voltage and RMS short-circuit current under different flag thickness and different channel width with rigid flagpole and flexible flagpole: (a) 10 mm channel width; (b) 20 mm channel width, and (c) 30 mm channel width.

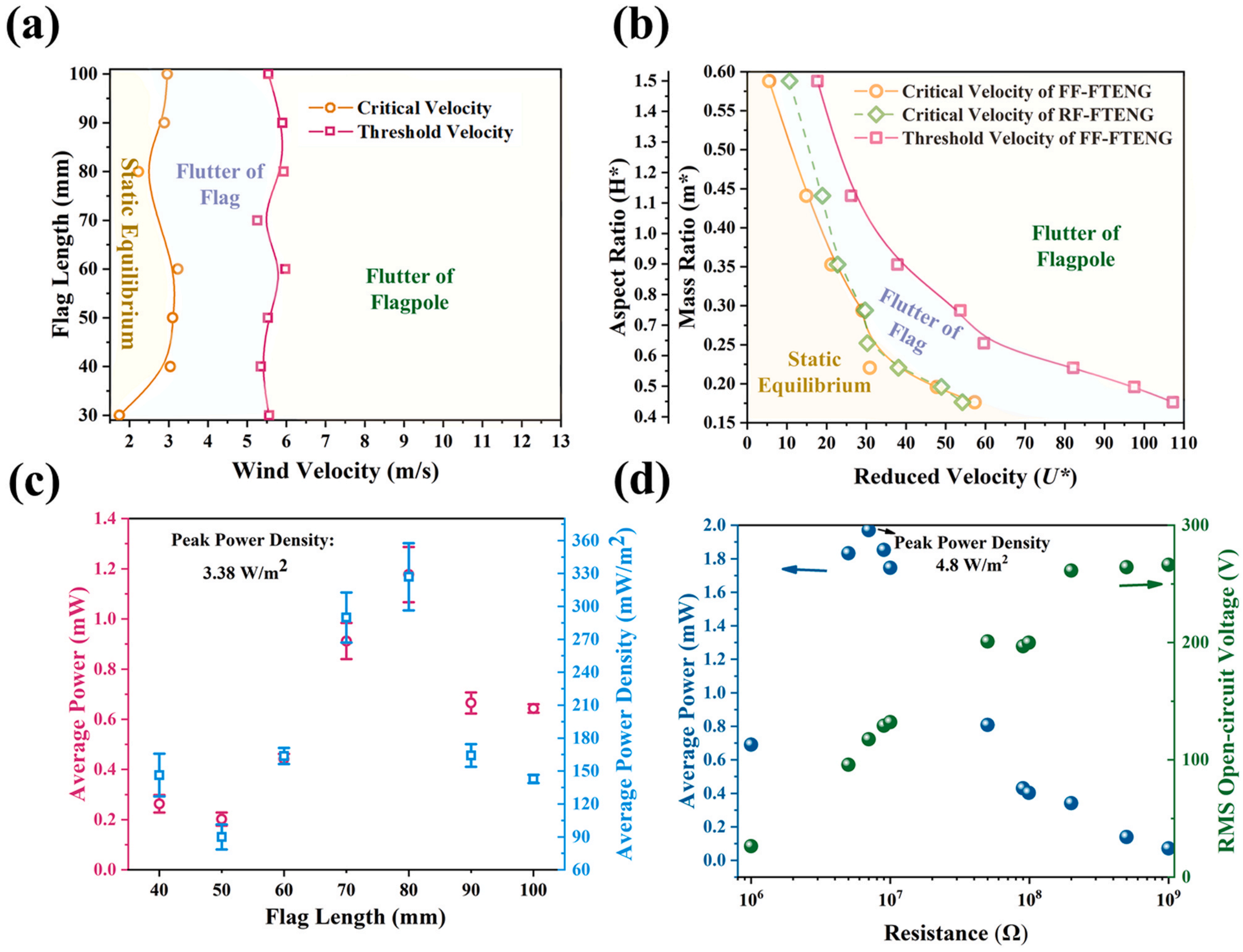

Fig. 7. (a) Dependence of critical velocity, threshold velocity and fluttering mode on flag lengths and wind velocity; (b) Fluttering mode of FF-FTENG and RF-FTENG; (c) Dependence of the optimal RMS power and RMS power density of the FF-FTENG on the flag length; (d) Dependence of RMS voltage and instantaneous power of FF-FTENG on the resistance of external load when the wind velocity is 10 m/s, the flag size is 45 mm (H) × 80 mm (L) and the channel width is 20 mm.

snapshot superimpositions of the FF-FTENG with different wind velocities from 6 to 12 m/s captured by a high-speed camera. The flagpole underwent an oscillation which amplified the flag's fluttering motion from 6 m/s. With increasing wind velocity, larger flag surfaces contacted with the PTFE walls and participated in the contact electrification and electrostatic induction processes. The fluttering amplitude of the leading edge of the flag enhanced with increasing wind velocities as indicated by the red arrows shown in Fig. 5(d). As shown in Fig. 5(e), there were two contact places between the flag and the sidewalls simultaneously (indicated by red lines in the figure), one contact place was made by the flag with the upper sidewall, another contact place was formed by the flag with the lower sidewall. According to the trajectory of the flag, the flag shape takes the form of a wave propagating in the wind direction, coupled to a spatial envelope $A(s)$. This phenomenon was also observed by other researchers [37–40]. Therefore, the spanwise oscillation of the flag can be approximately described as:

$$y(s,t) = A(s)\sin(2\pi ft + \frac{2\pi s}{\lambda}) \tag{3}$$

where s is the length along the flag from the leading edge, t is time, y is the displacement normal to the flow direction, $A(s)$ is the spatial envelope, f is the flapping frequency, and λ is the flapping wavelength. The waveform of the flag in FF-FTENG has been studied in another work from our group [41]. The contact places moved forward from the leading edge of the flag to the trailing edge of the flag. When the flow velocity increased from 8 m/s to 12 m/s as shown in Fig. 5(e), the contact areas were further enlarged.

doi:10.1016/j.nanoen.2021.106284

3.3. The performance of FF-FTENG under different channel width, flag thickness and flag length

In this section, two sets of experiments were presented. The first experiment studied the influence of flag thickness and channel width, while the influence of the flag length was investigated in the second experiment.

First, the performances of FF-FTENG with different flag thicknesses, h (20 μm, 30 μm and 70 μm), and channel widths, d (10 mm, 20 mm, and 30 mm), were tested under the same flag length $L = 80$ mm and the results are shown in Fig. 6. For all the channel widths, the electrical output of FF-FTENG with flag thicknesses of 20 μm, 30 μm and 70 μm significantly enhanced in terms of $V_{oc,RMS}$ and $I_{sc,RMS}$, compared to that of RF-FTENG. The optimal channel width was 20 mm, because the critical velocity was relatively high when the channel width was 10 mm, and the short-circuit current was low when the channel width was 30 mm.

As for the thickness, a thicker flag had larger $V_{oc,RMS}$ and $I_{sc,RMS}$ outputs in a wider channel: when the channel width was 10 mm, higher $V_{oc,RMS}$ and $I_{sc,RMS}$ were obtained for the flag with thickness of 20 μm than that of 30 μm, while higher voltage and current outputs were obtained by the flag with thickness of 30 μm when the channel width was 30 mm. When the channel width was 20 mm, higher $V_{oc,RMS}$ and $I_{sc,RMS}$

were obtained by the flag with thickness of 30 μm than the flag with thickness of 20 μm under a lower wind velocity. When the wind velocity increased to 7–9 m/s, larger $V_{oc,RMS}$ and $I_{sc,RMS}$ were obtained by the flag with thickness of 20 μm than the flag with thickness of 30 μm. However, the voltage and current of a flag with thickness of 70 μm are the lowest among all the three different channel widths. The influence of flag thickness in RF-FTENG is much more straight forward: a thicker flag performed better in terms of $V_{oc,RMS}$ and $I_{sc,RMS}$ for all the three different channel widths.

Second, a parametric study of the flag length was carried out as it was also a major factor that determines the electrical output of the FF-FTENGs. All the flags had the same width of 45 mm and thickness of 20 μm, while the channel width was 20 mm.

For the FF-FTENG, the critical velocity is between 1.5 and 3 m/s, and the threshold velocity is between 5 and 6 m/s with different flag lengths as shown in Fig. 7(a). To generalize the results, some dimensionless numbers are used in the analysis to characterize the fluttering mode of the FF-FTENG. They are mass ratio m^*, aspect ratio H^*, and reduced velocity U^* [21,42]. m^* is the ratio of the solid inertia to the fluid inertia. H^* is the ratio of the flag width to the flag length. U^* is the ratio of the kinetic energy of the incoming flow to the elastic energy of the flag. The equations to calculate these dimensionless numbers are as follows.

$$m^* = \rho h / \rho_a L \tag{4}$$

$$H^* = H/L \tag{5}$$

$$U^* = UL\sqrt{\frac{\rho_a HL}{B}} \tag{6}$$

where U is the wind velocity, ρ is the flag density (1062.1 kg/m^3), h is the flag thickness, ρ_a is the air density (1.204 kg/m^3), L is the flag length, H is the flag width, and B is the bending stiffness which can be calculated as $B = Eh^3H/12$, where E is the elastic modulus of the flag (4.82 GPa). The fluttering mode of flag in the FF-FTENG can be characterized in a two-dimensional space of dimensionless parameters (m^* and U^*) as shown in Fig. 7(b). Flags with larger m^* are prone to flutter at a lower U^* due to the destabilizing effects of inertia. In general, by increasing the incoming velocity above the stability boundary, the flag begins to flutter periodically. By further increasing the incoming velocity above the threshold boundary, the flagpole starts to flutter and the voltage and current generated from the FF-FTENG start to increase with a larger rate. We also compared the stability boundary of the FF-FTENG with that of the RF-FTENG. We found that the stability boundaries of the FF-FTENG and RF-FTENG are almost the same. Only when the mass ratio, or the aspect ratio, is large, the critical velocity of the RF-FTENG is a bit larger than that of the FF-FTENG. The threshold boundary of RF-FTENG doesn't exist because the rigid flagpole doesn't vibrate under the wind speeds considered.

In order to further understand the power output performance of the FF-FTENG with different flag lengths, the power and power density of different flag lengths were investigated at a wind velocity of 7 m/s as shown in Fig. 7(c). The wind velocity of 7 m/s was chosen because it is just above the threshold velocity for all flag lengths. For each point in Fig. 7(c), various external loads with resistance ranging from 1 MΩ to 1 GΩ were connected to the device to investigate the electrical power output of the FF-FTENG. The error bars represent standard deviations of the collected data. Clearly, the average power and average power density decreased a bit at the beginning and then gradually increased with the increasing flag length. The lowest power and power density took place when the flag length was 50 mm. The average power output of FF-FTENG with 40 mm and 50 mm flag was similar, however, since the area of 40 mm length flag is smaller, the FF-FTENG with 40 mm length flag had a larger power density. The smaller contact area was offset by its higher fluttering frequency as shown in Fig. S3 in the Supplementary Materials. The highest power density and highest average power for flag length are 80 mm. The FF-FTENG with a flag length of 80 mm had an average power of 1.07 mW and a peak power density of 3.38 W/m^2. However, further enhancement of the flag length decreased the power, as well as the power density. It is proposed that the reason why the 90 mm and 100 mm flags generated less energy than the 80 mm flag is that the fluttering of an extensively long flag lost its regularity and became random and chaotic. The complex fluttering decreases the contact areas between the flag and channel walls, which decreases the current output. Thus, the optimal flag length under the channel width of 20 mm is 80 mm flag.

Table 1
Comparison with previous FTENGs.

Triboelectric Materials	Voltage (V)	Power density (W/m^2)	Wind velocity (m/s)	Critical Velocity (m/s)	Ref.
CT and PTFE (this work)	348	4.8	10	2.23	
Al and FEP	100	0.029	10	6.5	[19]
Al and PTFE	300	1.87	7.6	–	[20]
CT and PTFE	200	0.023	15	2.8	[21]
Au-coated CT and structured PDMS	49	0.005	10	1.2	[22]
Ag and FEP	175	1.04	8	1.6	[44]
Cu and FEP	–	2.6	10	5	[45]
Al and PTFE	330	1.2	11	4	[46]
Cu and FEP	51	0.87	18	–	[12]
Al and PA	218	1.83	12	5.9	[47]
ITO and PET	98	2.8	27	6.2	[48]
Ag and FEP	70	0.6	7.5	4.5	[49]
Aluminium and PDMS	160	2.23	10.6	–	[50]

The wind velocity was further increased to test the energy output of the FF-FTENG under wind velocity of 10 m/s. As shown in Fig. 7(d), the FF-FTENG reached an average power of 1.97 mW and a peak power output of 17.3 mW (4.8 W/m^2) at 7 MΩ. By using the average power, the conversion efficiency was calculated to be 0.36%. The details about the definition and calculation of efficiency can be found in Supplementary Materials Note S3. However, for the RF-FTENG (Fig. S4 in Supplementary Materials), the average power was only 17.4 μW and the peak power output was only 0.583 mW (161.94 mW/m^2). The conversion efficiency of RF-FTENG is 0.003%. A 113 times enhancement of average power output was achieved.

3.4. Comparison with previous FTENGs

The power density and the critical velocity of the FF-FTENG were compared with other previous FTENGs which are reported in Table 1. Comparing with the previous works, the new FF-FTENG has a lower critical velocity as well as a higher power output. The critical velocity of FF-FTENG is less than 3 m/s, which means that the FF-FTENG can be used to harvest energy in some low-speed scenarios, such as human breathing, walking, running and HVAC [37]. In addition, all the materials in this design can be bought directly from the markets and no special material treatment was required. While FF-FTENG is proposed here as a novel structure design for optimizing the fluid-structure interaction, the electrical outputs of a FTENG can be further enhanced by using the novel materials introduced by other researchers to improve the surface charge density. This design is transferable to other FTEGN structures, since all the flags need to have a flagpole to sustain in the wind. In order to demonstrate that the flexible pole can be transferred to any other FTENG structures, a structure proposed by Wang et al. [20] was mimicked and reconstructed as shown in Fig. S5 in the Supplementary Materials. The energy output of this FTENG with flexible and rigid flagpole was compared and the results are shown in Table S3 in the Supplementary Materials. An enhancement of more than two folds

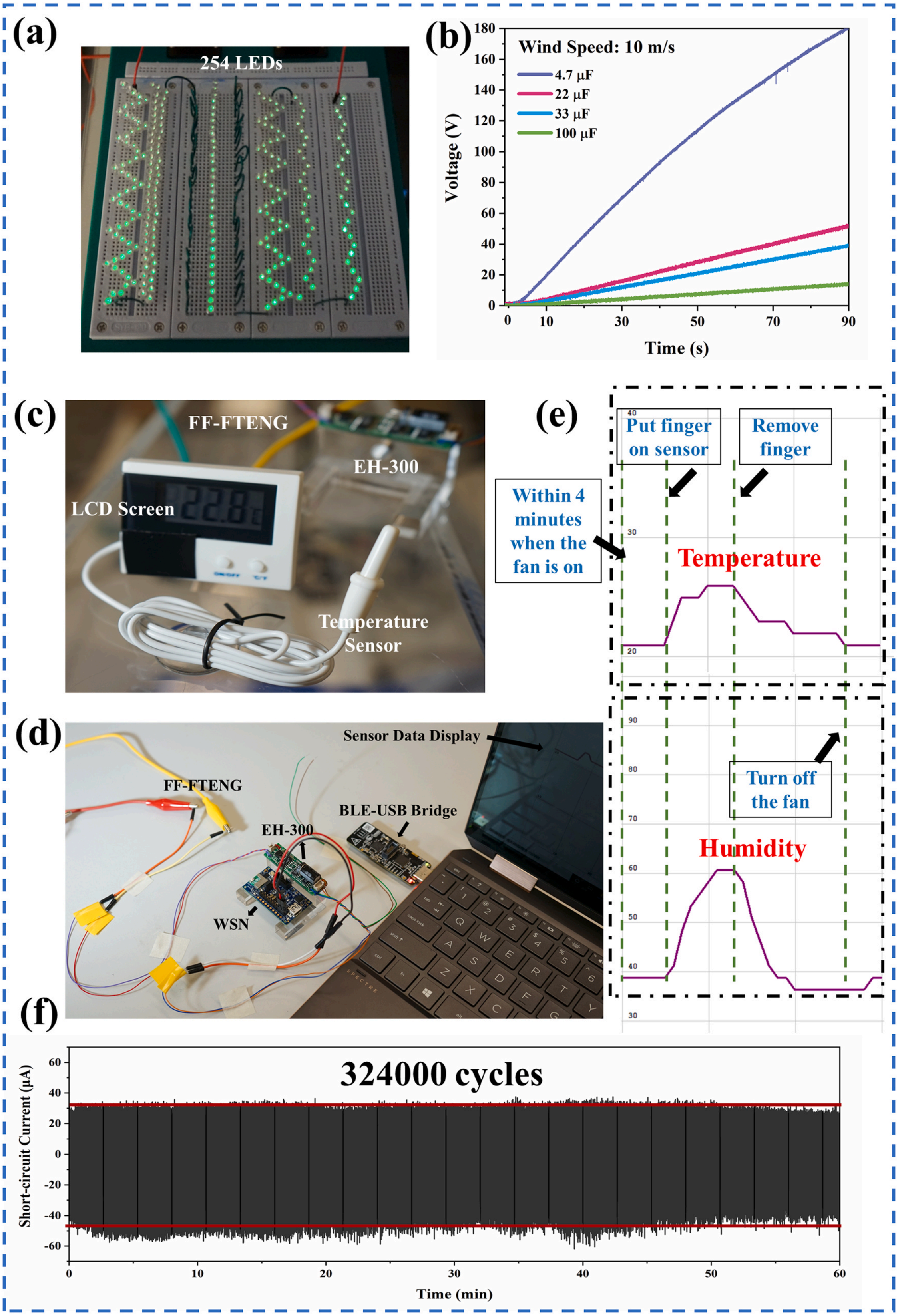

Fig. 8. (a) 254 LEDs were lit by a FF-FTENG under 10 m/s; (b) Measured voltage of the capacitor (4.7, 22, 33, and 100 μF) charged with a FF-FTENG at U= 10 m/s; (c) Photograph of a temperature sensor powered by a FF-FTENG; (d) Photograph of the self-powered WSN system including a FF-FTENG, a power management module EH-300, a wireless sensor node and a BLE-USB bridge; (e) Demonstration of the WSN system powered by a FF-FTENG for wireless signal transmission of temperature and humidity; (f) The one-hour durability test under 10 m/s flow velocity with continuous working cycles around 324,000.

($1.59\ \mathrm{W/m^2}$ to $3.38\ \mathrm{W/m^2}$) was achieved by using a flexible flagpole.

3.5. Demonstration

To illustrate the capability of the FF-FTENG as a practical power source for low-power electronic devices, two basic strategies to utilize the harvester energy were demonstrated, including 1. *immediate* and 2. *charge and release* [43]. For the *immediate use* strategy, 254 commercial green LEDs were successfully lit up by connecting in series to the FF-FTENG with flag size of 45 mm (H) × 80 mm (L) under the wind velocity of 10 m/s, as shown in Fig. 8(a) and Movie S2. However, considering the nature of the TENG's high voltage, low current and pulse peaks waveform [20], as well as the intermittent and irregular manner of wind energy, it is necessary to use a power management circuit to convert the high AC output of the FF-FTENG to a sustainable DC output for better practical applications, which is the *charge and release* strategy. Therefore, it was demonstrated that the output power of the FF-FTENG was stored in capacitors through a full-bridge rectifier. As shown in Fig. 8(b), four capacitors with different capacitance were successfully charged by the FF-FTENG under wind velocity of 10 m/s. The 4.7 μF capacitor took 90 s to charge to 180 V. Likewise, 22, 33 and 100 μF capacitors were charged to 53, 40, and 15 V within 90 s, respectively.

doi:10.1016/j.nanoen.2021.106284

Besides, a power management module (EH-300, Advanced Linear Devices, USA) was used (the mechanism of EH-300 is shown in Fig. S6 and Note S4 in the Supplementary Materials). With this circuit, the FF-FTENG can continuously power a digital temperature meter, as shown in Fig. 8(c). Even when the wind velocity is extremely low and there is no fluttering taking place, the energy stored in the module can continue to power the electronics for a while because of the stored energy in the EH-300 as shown in Fig. 8(d). The FF-FTENG can also power a WSN that transmits sensor data (temperature and humidity sensor, Si7020-A10) using a Bluetooth Low Energy Module (BLE, CYBLE-022001-00) through the EH-300. The signal can be received by a PC through Cypress BLE-USB Bridge (CY7C65213) as shown in Fig. 8(e). The robustness and durability of an energy harvesting device are of vital importance for its practical applications for continuous operation. The durability of the FF-FTENG device mainly depends on that of the flag material because of the cyclic impact motion. The abrasion of the PTFE walls is negligible. The tensile property of CT was measured by the SANS universal testing machine. The tensile stress as a function of strain is shown in Fig. S7. CT has a high ultimate strength of 161.72 MPa and a Young's modulus of 4.82 GPa. The density, Young's modulus and ultimate strength of the CT and other polymers are compared in Table S2 in the Supplementary Materials. In addition, the CT has high ultimate strength, which is only lower than Kapton among some common polymers. The high strength ensures the durability of the FF-FTENG under high wind velocity in long-term operation. To verify its durability, the current output was tested for prolonged fluttering behaviors. The result was shown in Fig. 8(f) and indicated that the current output of a 45 mm (H) × 80 mm (L) × 20 μm (h) flag did not change significantly even after a continuous 324,000 fluttering cycles (60 min) under wind velocity of 10 m/s.

4. Conclusions

In short, an innovative flutter-driven triboelectric nanogenerator (FTENG) with flexible flagpole to sustain the flag in the wind was designed. This FTENG exhibited a higher fluttering mechanical energy and generated more energy compared with traditional FTENG. The mechanism of motion amplification introduced by the flexible flagpole was explained through high-speed camera images. It was found that when the flag flutters, the flagpole also undergoes aerodynamic force. The lift force generated from the fluttering flag applies a periodic moment and a periodic force on the flagpole, causing the flagpole to vibrate. The vibration of the flagpole, in turn, amplifies the fluttering motion of the flag. The influence of the wind velocity, thickness of the flag, channel width and flag length were also investigated systematically. The highest energy output, as well as the lowest critical velocity, were obtained under the channel width of 20 mm. Thicker flag is preferred under low wind velocity and thinner flag is suitable to operate under high wind velocity. An optimal flag length of 80 mm was sought to achieve the highest power density among the flag length from 40 mm to 100 mm. The maximum power density of $4.8\ \mathrm{W/m^2}$ was achieved at load resistance of 7 MΩ under the wind velocity of 10 m/s. A 113 times enhancement of average power output was achieved compared to RF-FTENG under the same conditions. In the device demonstration, the harvester can light 254 LEDs and a temperature and humidity wireless sensor. Moreover, the FF-FTENG also exhibited stable output performance even after the long-term cyclic operation. The device has a lower critical velocity and higher energy outputs compared to most of the previous researches. In addition, our design can be transferred to other FTENG structures and achieved two-fold enhancement. Future work is needed to study how the threshold velocity related to the rigidity of flexible flagpole such that the threshold velocity of FF-FTENG can be further reduced and the FF-FTENG can have larger power output under breeze wind conditions (< 6 m/s). This flexible flagpole design opens a way to develop high-performance FTENG.

CRediT authorship contribution statement

Yi Zhang: Conceptualization, Methodology, Writing - original draft. **Sau Chung Fu:** Data curation, Writing – Review & Editing. Ka Chung Chan: Resources, Writing - review & editing. **Dong-Myeong Shin**: Data curation, Visualization. **Christopher Yu Hang Chao:** Supervision, Project administration, Funding acquisition.

Declaration of Competing Interest

The authors declare that they have no known competing financial interests or personal relationships that could have appeared to influence the work reported in this paper.

Acknowledgements

The work was supported by the General Research Fund (GRF) (project Nos. 17205419 & 17203220) granted by the Research Grants Council of the Hong Kong Special Administrative Region, China.

Appendix A. Supporting information

Supplementary data associated with this article can be found in the online version at doi:10.1016/j.nanoen.2021.106284.

References

[1] K.S. Adu-Manu, N. Adam, C. Tapparello, H. Ayatollahi, W. Heinzelman, Energy-harvesting wireless sensor networks (EH-WSNs) a review, ACM Trans. Sens. Netw. (TOSN) 14 (2018) 1–50.

[2] F.K. Shaikh, S. Zeadally, Energy harvesting in wireless sensor networks: A comprehensive review, Renew. Sustain. Energy Rev. 55 (2016) 1041–1054.

[3] K. Zhang, S. Wang, Y. Yang, A one-structure-based piezo-tribo-pyro-photoelectric effects coupled nanogenerator for simultaneously scavenging mechanical, thermal, and solar energies, Adv. Energy Mater. 7 (2017), 1601852.

[4] K. Zhang, Z.L. Wang, Y. Yang, Conductive fabric-based stretchable hybridized nanogenerator for scavenging biomechanical energy, ACS Nano 10 (2016) 4728–4734.

[5] T. Quan, Y. Yang, Fully enclosed hybrid electromagnetic–triboelectric nanogenerator to scavenge vibrational energy, Nano Res. 9 (2016) 2226–2233.

[6] H. Wang, Z. Xiang, P. Giorgia, X. Mu, Y. Yang, Z.L. Wang, C. Lee, Triboelectric liquid volume sensor for self-powered lab-on-chip applications, Nano Energy 23 (2016) 80–88.

[7] Y. Yang, H. Zhang, Z.L. Wang, Direct-current triboelectric generator, Adv. Funct. Mater. 24 (2014) 3745–3750.

[8] T. Quan, Y. Wu, Y. Yang, Hybrid electromagnetic–triboelectric nanogenerator for harvesting vibration energy, Nano Res. 8 (2015) 3272–3280.

[9] X. Liu, K. Zhao, Z.L. Wang, Y. Yang, Unity convoluted design of solid li-ion battery and triboelectric nanogenerator for self-powered wearable electronics, Adv. Energy Mater. 7 (2017), 1701629.
[10] L. Zhao, Y. Yang, Toward small-scale wind energy harvesting: design, enhancement, performance comparison, and applicability, Shock Vib. 2017 (2017) 1–31.
[11] B. Chen, Y. Yang, Z.L. Wang, Scavenging wind energy by triboelectric nanogenerators, Adv. Energy Mater. 8 (2018), 1702649.
[12] X. Wang, Y. Yang, Effective energy storage from a hybridized electromagnetic-triboelectric nanogenerator, Nano Energy 32 (2017) 36–41.
[13] K. Zhao, Y. Yang, X. Liu, Z.L. Wang, Triboelectrification-enabled self-charging lithium-ion batteries, Adv. Energy Mater. 7 (2017), 1700103.
[14] G. Xu, X. Li, X. Xia, J. Fu, W. Ding, Y. Zi, On the force and energy conversion in triboelectric nanogenerators, Nano Energy 59 (2019) 154–161.
[15] M. Cai, J. Wang, W.-H. Liao, Self-powered smart watch and wristband enabled by embedded generator, Appl. Energy 263 (2020), 114682.
[16] A. Moschitta, I. Neri, Power consumption assessment in wireless sensor networks, ICT-energy-concepts towards zero-power information and communication technology, IntechOpen (2014).
[17] K.S.D. Gunawardhana, N.D. Wanasekara, R.I.G. Dharmasena, Towards truly wearable systems: optimizing and scaling up wearable triboelectric nanogenerators, Iscience 23 (2020), 101360.
[18] K.E. Byun, M.H. Lee, Y. Cho, S.G. Nam, H.J. Shin, S. Park, Potential role of motion for enhancing maximum output energy of triboelectric nanogenerator, APL Mater. 5 (2017), 074107.
[19] Y. Yang, G. Zhu, H. Zhang, J. Chen, X. Zhong, Z.H. Lin, Y. Su, P. Bai, X. Wen, Z. L. Wang, Triboelectric nanogenerator for harvesting wind energy and as self-powered wind vector sensor system, ACS nano 7 (2013) 9461–9468.
[20] S. Wang, X. Mu, Y. Yang, C. Sun, A.Y. Gu, Z.L. Wang, Flow-driven triboelectric generator for directly powering a wireless sensor node, Adv. Mater. 27 (2015) 240–248.
[21] J. Bae, J. Lee, S. Kim, J. Ha, B.-S. Lee, Y. Park, C. Choong, J.-B. Kim, Z.L. Wang, H.-Y. Kim, J.-J. Park, U.I. Chung, Flutter-driven triboelectrification for harvesting wind energy, Nat. Commun. 5 (2014) 4929.
[22] B. Dudem, D.H. Kim, J.S. Yu, Triboelectric nanogenerators with gold-thin-film-coated conductive textile as floating electrode for scavenging wind energy, Nano Res. 11 (2018) 101–113.
[23] X. Wang, S. Wang, Y. Yang, Z.L. Wang, Hybridized electromagnetic–triboelectric nanogenerator for scavenging air-flow energy to sustainably power temperature sensors, ACS Nano 9 (2015) 4553–4562.
[24] M. Xu, Y.C. Wang, S.L. Zhang, W. Ding, J. Cheng, X. He, P. Zhang, Z. Wang, X. Pan, Z.L. Wang, An aeroelastic flutter based triboelectric nanogenerator as a self-powered active wind speed sensor in harsh environment, Extrem. Mech. Lett. 15 (2017) 122–129.
[25] H. Phan, D.M. Shin, S. Heon Jeon, T. Young Kang, P. Han, G. Han Kim, H. Kook Kim, K. Kim, Y.-H. Hwang, S. Won Hong, Aerodynamic and aeroelastic flutters driven triboelectric nanogenerators for harvesting broadband airflow energy, Nano Energy 33 (2017) 476–484.
[26] S. Cho, Y. Shin, J. Choi, J. Eom, B.S. Oh, J. Lee, G.Y. Jung, Triboelectric nanogenerator based on intercalated Al layer within fluttering dielectric film, Nano Energy 77 (2020), 105184.
[27] H. Lin, M. He, Q. Jing, W. Yang, S. Wang, Y. Liu, Y. Zhang, J. Li, N. Li, Y. Ma, Angle-shaped triboelectric nanogenerator for harvesting environmental wind energy, Nano Energy 56 (2019) 269–276.
[28] Z. Ren, Z. Wang, Z. Liu, L. Wang, H. Guo, L. Li, S. Li, X. Chen, W. Tang, Z.L. Wang, Structure, morphology, and photoelectric performances of Te-Sb2Se3 thin film prepared via magnetron sputtering, Nanomater. (Basel, Switz.) 10 (2020), 2001770.
[29] E. Virot, X. Amandolese, P. Hémon, Fluttering flags: an experimental study of fluid forces, J. Fluids Struct. 43 (2013) 385–401.
[30] E. Virot, Flottement de drapeau: dynamique et couplage, Ph.D. Thesis, Éc. Polytech. (2015).
[31] E. Virot, D. Faranda, X. Amandolese, P. Hémon, Chaotic dynamics of flags from recurring values of flapping moment, Int. J. Bifurc. Chaos 27 (2017), 1750020.
[32] E. Virot, X. Amandolese, P. Hémon, Coupling between a flag and a spring-mass oscillator, J. Fluids Struct. 65 (2016) 447–454.
[33] Q. Fu, Y. Chen, M. Sorieul, Wood-based flexible electronics, ACS Nano 14 (2020) 3528–3538.
[34] T. Crompton, Mechanical properties of polymers, Smithers Rapra Technology Ltd., Shropshire, 2012.
[35] S. Niu, S. Wang, L. Lin, Y. Liu, Y.S. Zhou, Y. Hu, Z.L. Wang, Theoretical study of contact-mode triboelectric nanogenerators as an effective power source, Energy Environ. Sci. 6 (2013) 3576–3583.
[36] L. Lin, Y. Xie, S. Wang, W. Wu, S. Niu, X. Wen, Z.L. Wang, Triboelectric active sensor array for self-powered static and dynamic pressure detection and tactile imaging, ACS Nano 7 (2013) 8266–8274.
[37] M. Perez, S. Boisseau, M. Geisler, P. Gasnier, J. Willemin, G. Despesse, J. Reboud, Aeroelastic flutter energy harvesters self-polarized by triboelectric effects, Smart Mater. Struct. 27 (2017), 014003.
[38] J. Allen, A. Smits, Energy harvesting eel, J. Fluids Struct. 15 (2001) 629–640.
[39] L.B. Jia, X.Z. Yin, Passive oscillations of two tandem flexible filaments in a flowing soap film, Phys. Rev. Lett. 100 (2008), 228104.
[40] Y.W. Hu, L.H. Feng, J.J. Wang, Passive oscillations of inverted flags in a uniform flow, J. Fluid Mech. 884 (2020) A32.
[41] Y. Zhang, K.C. Chan, S.C. Fu, C.Y.H. Chao, Fluttering amplitude amplification by utilizing flapping moment in flutter driven triboelectric nanogenerator, Proceedings of the ASME 2021 15th International Conference on Energy Sustainability, ASME, Virtual, Online, 2021.
[42] X. Wang, S. Alben, C. Li, Y.L. Young, Stability and scalability of piezoelectric flags, Phys. Fluids 28 (2016), 023601.
[43] M.E. Karagozler, I. Poupyrev, G.K. Fedder, Y. Suzuki, Paper generators: harvesting energy from touching, rubbing and sliding, Proc. 26th Annu. ACM Symp. Use Interface Softw. Technol. (2013) 23–30.
[44] X. Chen, X. Ma, W. Ren, L. Gao, S. Lu, D. Tong, F. Wang, Y. Chen, Y. Huang, H. He, B. Tang, J. Zhang, X. Zhang, X. Mu, Y. Yang, A triboelectric nanogenerator exploiting the bernoulli effect for scavenging wind energy, Cell Rep. Phys. Sci. 1 (2020), 100207.
[45] Y. Wang, J. Wang, X. Xiao, S. Wang, P.T. Kien, J. Dong, J. Mi, X. Pan, H. Wang, M. Xu, Multi-functional wind barrier based on triboelectric nanogenerator for power generation, self-powered wind speed sensing and highly efficient windshield, Nano Energy 73 (2020), 104736.
[46] Y. Bian, T. Jiang, T. Xiao, W. Gong, X. Cao, Z. Wang, Z.L. Wang, Triboelectric nanogenerator tree for harvesting wind energy and illuminating in subway tunnel, Adv. Mater. Technol. 3 (2018), 1700317.
[47] K. Zhao, Z.L. Wang, Y. Yang, Self-powered wireless smart sensor node enabled by an ultrastable, highly efficient, and superhydrophobic-surface-based triboelectric nanogenerator, ACS nano 10 (2016) 9044–9052.
[48] L. Zhang, B. Zhang, J. Chen, L. Jin, W. Deng, J. Tang, H. Zhang, H. Pan, M. Zhu, W. Yang, Z.L. Wang, Lawn structured triboelectric nanogenerators for scavenging sweeping wind energy on rooftops, Adv. Mater. 28 (2016) 1650–1656.
[49] W. Sun, Z. Ding, Z. Qin, F. Chu, Q. Han, Wind energy harvesting based on fluttering double-flag type triboelectric nanogenerators, Nano Energy 70 (2020), 104526.
[50] Q. Zhou, J.-N. Kim, K.-W. Han, S.-W. Oh, S. Umrao, E.J. Chae, I.-K. Oh, Integrated dielectric-electrode layer for triboelectric nanogenerator based on Cu nanowire-Mesh hybrid electrode, Nano Energy 59 (2019) 120–128.

Yi Zhang received his B.S. degree from Xi'an Jiaotong University in 2017 and MPhil degree from The Hong Kong University of Science and Technology (HKUST) in 2019. He is currently a Ph.D. candidate at the Department of Mechanical Engineering at the University of Hong Kong. His research interests include fluttering phenomenon, triboelectric nanogenerator, and green building techniques.

Dr. Sau-chung Fu is a research assistant professor in the Department of Mechanical Engineering, HKU. He received his BEng and MPhil in Mechanical Engineering from the University of Hong Kong in 1999 and 2001 respectively. After practiced for some years in an engineering consultant, he went on pursuing a Ph.D. degree in Mechanical Engineering at the Hong Kong Polytechnic University in 2011. Dr. Fu's research focused on aerosol and bioaerosol, nanofluids and heat exchanger, turbulent flow, computational fluid dynamics, wind power systems, and ventilation systems.

Dr. Oscar K.C. Chan is a Postdoctoral Scholar at The University of Hong Kong. He received his Bachelor's, MPhil and Ph.D. degree in Mechanical Engineering from The Hong Kong University of Science and Technology in 2009, 2011 and 2015, respectively. His research area includes energy and thermal systems, adsorption technology, energy sustainability and thermal fluidic simulation.

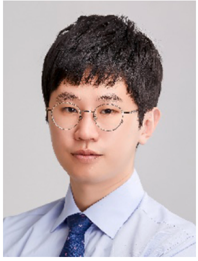

Dong-Myeong Shin is an Assistant Professor of Mechanical Engineering at the University of Hong Kong. He obtained B.S. (2009) M.S. (2011) and Ph.D. (2016) in nanomaterials from Pusan National University under supervision of Prof. Yoon-Hwae Hwang and Prof. Hyung Kook Kim. In 2017, he moved to the University of California, Berkeley as a postdoctoral scholar with Prof. Jeffrey R. Long. Upon completion of his postdoctoral studies in 2019, Dong-Myeong traveled back to Asia to assume his current position and his group has devoted to developing the self-powered nanoelectronics, with an emphasis on important components such as energy harvesting/storage devices.

Prof. Christopher Y.H. Chao is Dean of Engineering and Chair Professor of Mechanical Engineering at The University of Hong Kong (HKU). He received his B.Sc.(Eng) degree in Mechanical Engineering (First Class) from HKU in 1988. He obtained his M.S. and Ph.D. degrees in Mechanical Engineering from The University of California, Berkeley, USA, in 1992 and 1994, respectively. He has a wide range of research interests in the areas of built environment, energy and environmental engineering. He is a fellow of a number of professional societies (FASME, FIMechE, FCIBSE, FISIAQ, FHKEng, FHKIE).